Isolation and Detection of Arc Fault Noise in a Real PV System Using Current Demodulation and Autocorrelation Coefficients

Jonathan C. Kim, Roy Ball, *Member, IEEE*, and Brad Lehman, *Fellow, IEEE*

***Abstract*—The safety, reliability, and efficiency of photovoltaic (PV) systems hinge on effective arc fault identification and detection. This research presents a new online current demodulation algorithm to filter the switching signal injected into the dc side of the inverter. Therefore, the detection algorithm adapts performance in real-time so that it can accurately detect an arc fault without being confused with unknown inverter harmonics or other unwanted tripping events. This increases robustness of the arc fault detector. The article provides deep theoretical analysis and explanation of the arc fault detection algorithm. It is also verified in 1) an experimental PV array using various commercial inverters with different pulsewidth modulation (frequencies and 2) data captured by Sandia National Laboratories.**

***Index Terms*—Arc discharges, fault detection, fault diagnosis, photovoltaic systems, power system reliability.**

I. Introduction

SERIES dc arc faults represent a hazardous class of faults in photovoltaic (PV) systems, capable of igniting flammable material around the fault location. Detecting arc faults accurately, while minimizing false alarms and unwanted shutdowns is crucial for reducing downtime, achieving expected energy output, and discovering genuine arc faults. A reliable arc fault detection device (AFDD) must be able to properly identify and differentiate arc fault conditions from normal PV operating conditions and other external disturbances. Although series dc arc faults by themselves are relatively easy to detect, the challenge lies in accurately distinguishing the arc fault from the various operational behaviors exhibited by PV systems [1], [2], [3].

This research addresses critical challenges in the field of arc fault detection within PV systems. It involves the purposeful induction of arc faults in a functioning PV system that is tested with three different string inverters. Within the commercial sector, there are recognized hurdles associated with arc fault detection devices that warrant effective solutions, which are as follows.

1) One significant challenge is the consistent tripping of many AFDD systems, particularly during system startup or when subjected to abrupt changes in irradiance on a string inverter. This issue underscores the need for improved detection reliability [2], [4], [5].
2) Most commercial PV AFDDs are commonly designed for inverters operating at narrow and known pulsewidth modulation (PWM) switching frequency ranges. However, when inverters with unknown PWM frequencies are integrated into the system, they can lead to false alarms [1], [6], [7], [8]. The PWM noise confuses the AFDD. Solving this frequency compatibility challenge is essential for enhanced AFDD performance.
3) Another persistent challenge revolves around the failure of AFDD systems to meet specified time clearing mandates for arc fault detection within PV systems, especially under conditions of low PV currents, such as shading or low light [1], [9]. This emphasizes the importance of refining detection algorithms to address these scenarios effectively.

This research contributes to tackling these pressing challenges in the commercial PV industry, offering insights and solutions to enhance the reliability and performance of arc fault detection systems.

Arc faults inject a power spectral density (PSD) characteristic proportional to $1/f$, called pink noise, where f is the frequency [3], [10]. The magnitude of the injected pink noise can be affected by different electrode characteristics such as material composition, geometry, current and voltage levels, and arcing state [11], [12], [13]. The effective arcing frequency band is widely recognized to be between 0 Hz and 100 kHz [6], [14]. However, many detection algorithms only use a narrow bandwidth or a select frequency inside the arcing frequency spectrum. Therefore, they are susceptible to false alarms that the algorithm was not specifically tuned to avoid or unexpected noise that falls inside the observed arcing frequency window.

In [6], a discrete wavelet transform (DWT) is designed to detect the arcing frequencies from between 31.3 and 62.5 kHz and avoid switching frequencies under 20 kHz. However, some string inverters do have switching frequencies at 30 kHz and above that may cause false alarms [16]. In [17], a time-domain characteristic such as a current magnitude change is used to indicate a potential arc fault using DWT and wavelet packet

Manuscript received 12 November 2023; revised 29 January 2024 and 15 March 2024; accepted 11 April 2024. Date of publication 19 April 2024; date of current version 20 June 2024. This work was supported and funded by Mersen, USA. An earlier version of this paper was presented at the 2022 IEEE Energy Conversion Congress and Exposition (ECCE), Detroit, MI, USA, 2022 [DOI: 10.1109/ECCE50734.2022.9947524]. Recommended for publication by Associate Editor G.-S. Seo. *(Corresponding author: Jonathan C. Kim.)*

Jonathan C. Kim and Brad Lehman are with Northeastern University, Boston, MA 02115 USA.

Roy Ball is with Mersen, Newburyport, MA 01950 USA.

Color versions of one or more figures in this article are available at https://doi.org/10.1109/TPEL.2024.3391420.

Digital Object Identifier 10.1109/TPEL.2024.3391420

decomposition (WPD). However, current magnitude changes are not unique to an arc fault and can be caused by other external factors, such as partial shading, irradiance changes, dc disconnect switch operations and load changes. In [18], the detected frequency range used to detect the arc fault is ten magnitudes lower, between 150 and 750 Hz, in order to avoid the switching frequency of the inverter. The algorithm utilizes a moving average and fast Fourier transform (FFT) to determine magnitude variations in the arc fault impedance characteristics. However, only part of the arc frequency spectrum is observed.

The pink noise characteristic of arc faults can quantify the chaotic nature of the arc fault. In [19], the Tsallis entropy is used to quantify disorder of the measured current signal to observe fast changing noise signatures to identify the presence of pink noise. In [10], the Hurst exponent is used to detect high-impedance dc arcing events and their measure of chaotic current behavior. Although entropy analysis of the current signal can detect arc faults, signal conditioning is favorable to eliminate any other noise signatures on the measured current to decrease the chance of false alarms.

In [20] and [21], multiple frequency bands are taken as inputs mitigate the influence of the switching frequency, EMI, and other background noise. However, there are further studies needed to determine the efficient number of frequency bands for detection and the number of elements and samples available influence the reliability of the arc fault detection.

Machine learning (ML) algorithms help determine the most useful detection parameters in hidden variables while utilizing a large signal database for training. In [22], an ensemble ML technique is discussed to extract useful arc fault features under different load types and optimize the classification of arc faults. However, ML techniques are heavily dependent on the size of the dataset, data consistency and reliability, model complexity, and interpretability [23].

In [24] and [25], the PV system configuration is utilized to determine abnormal system behaviors using the intrinsic sensors available in the module level dc/dc converter or dc optimizers to improve the cost effectiveness of the detection solution. Typical arc fault behavior is observed by analyzing the operating point behavior of the voltage signal as the arc fault interacts with the differential power processing structure utilized in the dc optimizers. However, this strategy is specific to the dc optimizer structure and not applicable to other PV system configurations.

The arc fault detection algorithm introduced in this article effectively isolates the arc fault frequency spectrum with different string inverter PV systems, without the need to specifically tune the search to a narrow bandwidth. Instead of directly tuning the arc fault detector bandwidth, it leverages current demodulation algorithms to eliminate undesired harmonics while preserving the pink noise characteristics of arc faults. This article extends the results of the preliminary conference paper by Kim et al. [26] by adding theoretical justification and improved current demodulation algorithms for the arc fault detection algorithms, along with expansive experimental implementations on a real PV installation. Specifically, research contributions of this article include the following.

1) *A new online search algorithm, current demodulation:* The proposed algorithm effectively filters out periodic noise and ripple from the current signal measurement, all without prior knowledge of the string inverter switching parameters. This contribution is essential as it lays the foundation for reliable signal processing, overcoming the challenge of dealing with varying and unknown parameters AFDD.
2) *Isolation and detection of a wide-bandwidth pink noise spectrum of the arc fault:* Unlike conventional techniques such as FFT, DWT, and WPD, this method employs differenced autocorrelation coefficient analysis. It allows for capturing a broader range of frequencies associated with arc faults. This is important because it enhances the algorithm's sensitivity and robustness, ensuring that even subtle arc fault noise characteristics are not missed.
3) *Simple outlier detection rules:* Straightforward rules have been established for identifying and disregarding single transient events and unwanted tripping conditions. These rules help prevent false alarms triggered by factors like current magnitude changes, load variations, dc switch operations, and sudden shifts in irradiance. This contribution is crucial as it improves the algorithm's reliability in real-world scenarios, reducing unnecessary system disruptions.
4) *Experimental validation of the proposed arc fault detection algorithm:* Through rigorous testing on real photovoltaic systems with different string inverters, the effectiveness and robustness of the algorithm have been demonstrated. This contribution is of paramount importance as it provides empirical evidence of the algorithm's practical utility, bridging the gap between theoretical development and real-world application.

The rest of this article is organized as follows. Section II introduces the arc fault frequency analysis and outlier elimination techniques. Section III discusses the arc fault detection algorithm and criteria. Section IV presents the experimental results validating the detection algorithm, and finally, Section V concludes this article and discusses future work.

II. Arc Fault Frequency Analysis

Unwanted tripping or masking of the arcing noise can be caused by MPPT in the dc–dc converter and/or switching frequency injected by the PV string inverter [3]. Current demodulation and differenced autocorrelation coefficient analysis is proposed in this research to eliminate signals that may cause unwanted tripping and false alarms and isolate the pink noise characteristic to accurately characterize the arc fault while ignoring other background noises. The major steps in the proposed arc fault detection algorithm are shown in Fig. 1.

A. Experimental Setup

Most detection algorithms require a priori knowledge of the PV system to effectively tune the band-pass filter and DWT for selecting an appropriate arcing frequency band in detection while avoiding the inverter switching frequency [17], [27], [28]. One major disadvantage is that the utilized arc fault frequency band is narrow and does not capture the pink noise characteristic of the arc fault PSD. The entropy methods discussed before

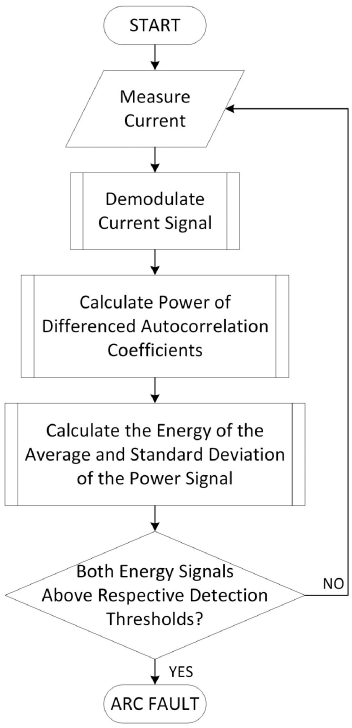

Fig. 1. Overview of the proposed arc fault detection algorithm.

attempt to isolate the chaotic nature in a single step without signal conditioning of the current signal [10], [19], [29].

The summation of different kinds of switching noise onto arc faults generated by off-grid and grid-tied PV systems are considered in this article. The off-grid PV system schematic is given in Fig. 2(a). The off-grid PV system includes a charge-controller unit which performs the MPPT and maintains a 48 V dc bus. The power is either directed to charge a battery or feed an ac load through an inverter unit. The arc fault can be generated in series at any location between the PV modules in the PV array. The PV array generates a maximum power of 1.2 kW with an ac output of a single-phase 120 V_{rms} at 60 Hz.

The schematic of the grid-tied PV system is given in Fig. 2(b) and a block diagram of the grid-tied PV system configurations is given in Fig. 3. The grid-tied PV system can be configured to either two parallel PV strings of six series connected PV panels or a single PV string with 12 PV panels in series for an output power of 3.9 kW. In addition, two different grid-tied inverters can be switched on one at a time to test the effect of different string inverters. Inverter A has a switching frequency of 20 kHz and Inverter B has a switching frequency of 32 kHz. A resistive load bank is available to sink the power generated by the PV system.

In addition, the operation of two commercial AFDD (Commercial AFDD A and Commercial AFDD B) was observed while gathering arc fault data. These are standalone devices using current sensors on a single PV string which send a disable signal to the inverter to stop operation once an arc fault is detected. The commercial devices are placed in series with the measurement device used for the proposed detection algorithm and the results are compared in Section V.

B. Current Demodulation Operation

Current demodulation is proposed to eliminate periodic noise and low-frequency DC trends, yielding a zero-meaned signal suitable for autocorrelation analysis. This approach effectively filters out the single-phase 120 Hz rectified ripple and PWM switching frequency noise originating from the PV system's string inverter, all while preserving the essential pink noise characteristics of arc fault noise. Consequently, the effectiveness of the proposed arc fault detection algorithms remains consistent, regardless of the inverter switching frequency within the PV system, as the demodulated signal remains free from the harmonics that could trigger false alarms.

Current demodulation is defined as the operation of subtracting a time-shifted copy of itself with the original signal. If the time-shift is equal to the period of the periodic signal, deconstructive interference occurs eliminating the periodic signal. This process is analogous to a smoothed derivative operation as in the following:

$$\underbrace{\frac{1}{\Delta t}\left(1-z^{-\Delta t}\right)}_{\text{Time - Shifted Subtraction}} = \ldots$$

$$\ldots \underbrace{\frac{1}{\Delta t}\left(1+z^{-1}+z^{-2}+\cdots+z^{-(\Delta t-1)}\right)}_{\text{Moving Average}} \underbrace{\left(1-z^{-1}\right)}_{\text{Differencing Operation}} \tag{1}$$

where Δt is the discrete time-shift, $(1-z^{-\Delta t})$ is the operation of subtracting the original signal "1" by the time-shifted signal, $z^{-\Delta t}$, through the z-transformation. The averaging operation acts as a low-pass filter with significant side-lobes determined by the time-shift as given in the following:

$$f_{\text{notch}} = \frac{f_s}{\Delta t} \tag{2}$$

where f_{notch} is the location of the first notch of the side-lobes and f_s is the sampling frequency of the measured current signal. The subsequent notch locations are multiples of f_{notch}. In addition, the differencing operation generates a null at the dc component generating a zero-meaned signal. In Fig. 4, the current demodulation operation is performed on an ideal pink noise PSD (black). The demodulated PSD (blue) shows the side-lobes which can be tuned to eliminate peaks generated by switching noise and a null at the dc component eliminating any dc components. Lastly, the average shape of the pink noise present in the system is preserved. Therefore, arc fault noise that is present in the shape of pink noise will be preserved while switching frequencies and other periodic noise can be eliminated.

The current demodulation operation is performed recursively, as a function of the time-shift, as an online search method of periodic noise. When the optimal time-shift, Δt_{opt}, is not used, the periodic signal present in the current signal is not eliminated through deconstructive interference. In Fig. 5(a), the dc component, switching noise and harmonics are present in a PV system. In Fig. 5(b), the original signal (black) is time-shifted to some nonoptimal time-shift (red). Therefore, although the differencing operation eliminates the dc component and the moving average operation performs a low-pass filtering effect to

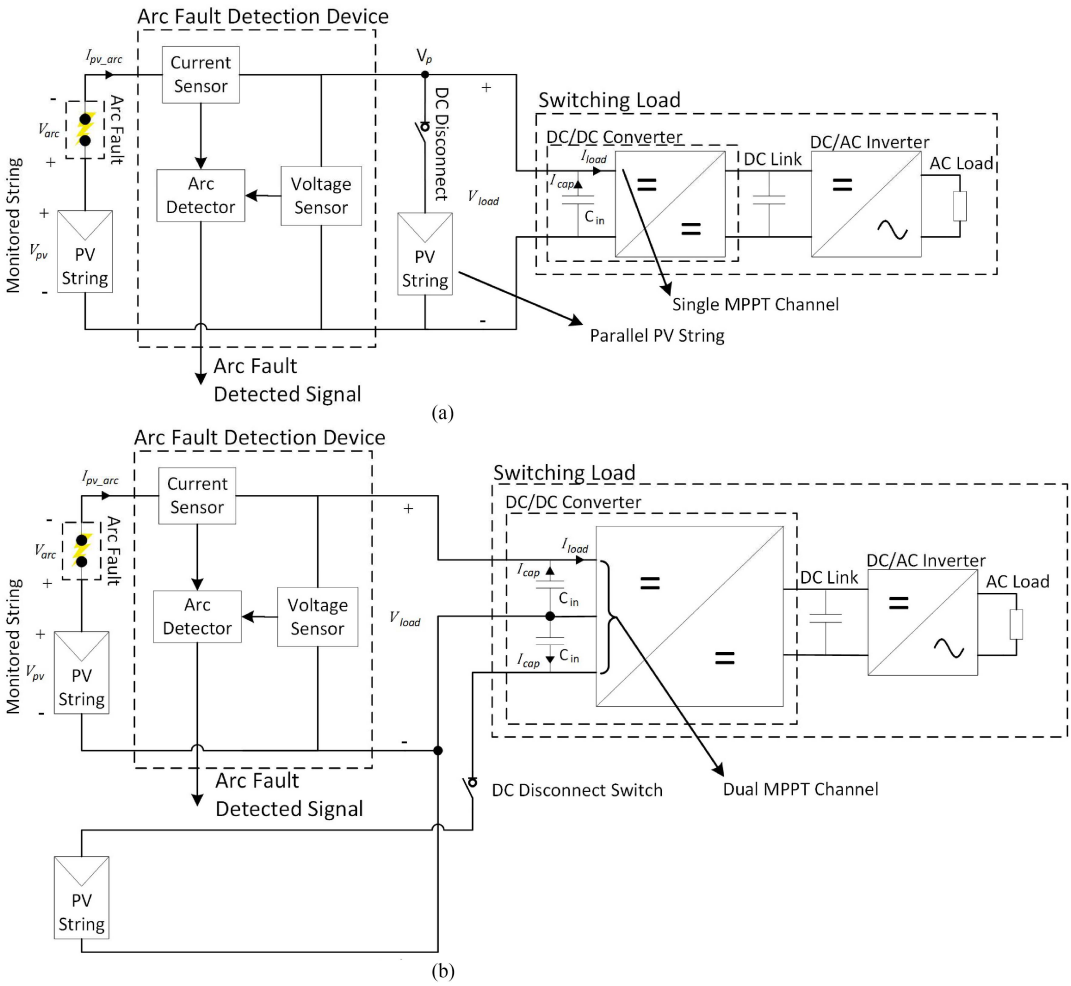

Fig. 2. (a) Schematic of off-grid PV system. (b) Schematic of grid-tied system.

eliminate some harmonics, the switching frequency still exists as a large component in the PSD (red) as shown in Fig. 5(c). In Fig. 5(d), the resulting current demodulated signal (red) still contains fluctuations from the periodic component.

However, when the time-shift is optimized for the switching frequency, $\Delta t = \Delta t_{\text{opt}}$, the time-shifted signal (green) is in phase with the original signal (black), in Fig. 5(b). Therefore, the switching component is eliminated (green) in Fig. 5(c) and there is no periodic signal present in the demodulated current signal (green) in Fig. 5(d).

C. Signal Conditioning Algorithm

As shown in Fig. 6, the signal conditioning algorithm utilizes the current demodulation operation to filter the current signal, instead of using a narrow-band-pass filter. The current signal, $i_k(t)$, is measured and then time-shifted by Δt_k, where k is the index of the first time-shift. The lengths of the time-shifted current, $i'_k(t)$, and original current signal are padded with zeros for vector calculations and then each corresponding time indexed is subtracted from each other. The standard deviation of the differenced current signal, $i_{\text{diff},k}(t)$, is calculated and compared to the standard deviation of the previous time-shift index differenced current signal, $i_{\text{std}}(k-1)$. The measured current signal is tested in discrete steps, t_{step}, between the minimum and maximum time-shift, $\Delta t_{\min} < \Delta t_k + t_{\text{step}} < \Delta t_{\max}$. The time-shift with the smallest standard deviation is considered the optimal solution and labeled as the demodulated current.

The minimum and maximum time-shift values correspond to the maximum and minimum inverter switching frequencies expected in the PV system, respectively. The optimal time-shift is determined by searching through the minimum and maximum time-shift boundaries and choosing the demodulated current signal with the smallest standard deviation. The standard deviation is large because of the amplitude of the periodic component. Conversely, when the dominating amplitude from the periodic component is minimized, the standard deviation will also be at a minimum.

D. Autocorrelation Coefficient Analysis

After the current signal has been conditioned and the periodic noise has been eliminated, the pink noise characteristic of the arc fault can be easily extracted without errors from other

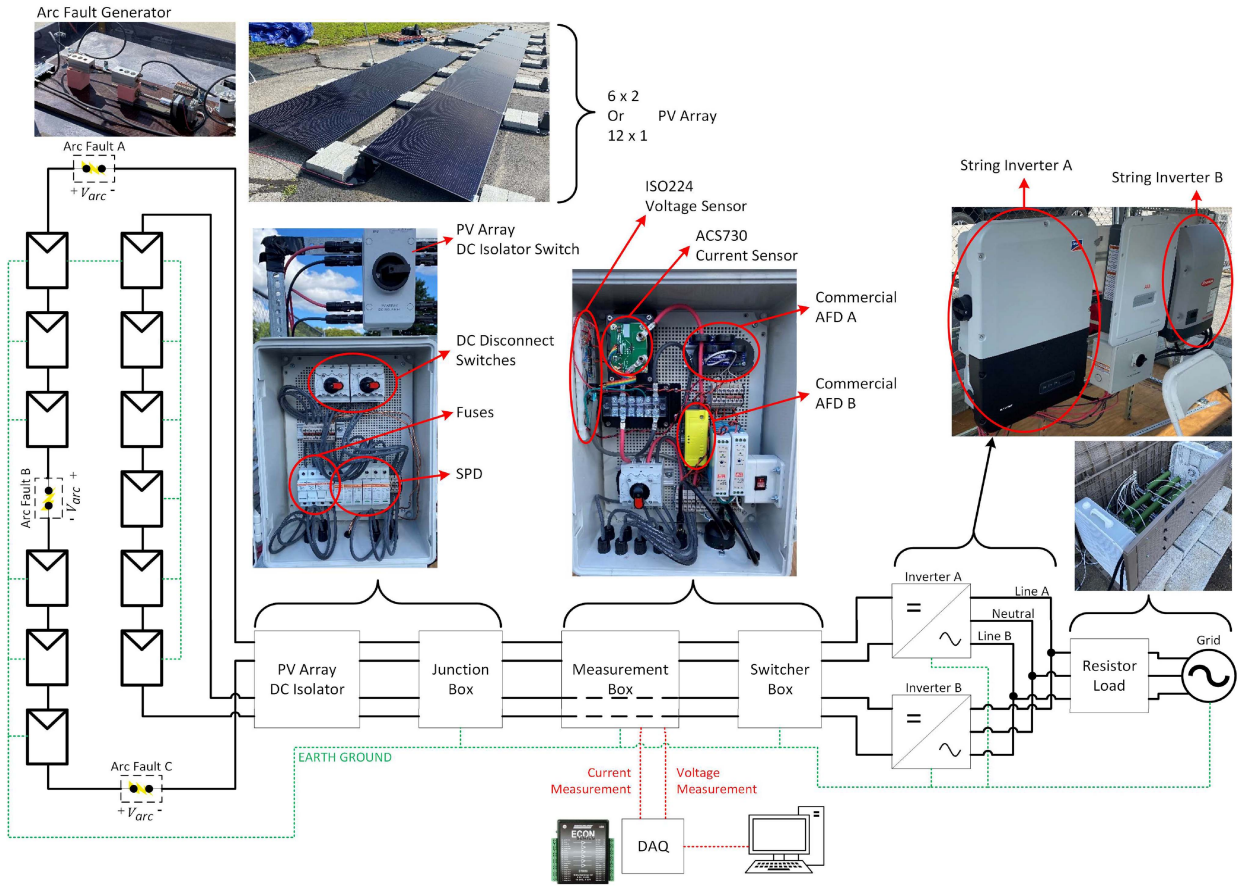

Fig. 3. Experimental setup and schematic of outdoor 3.9 kW grid-tied PV system.

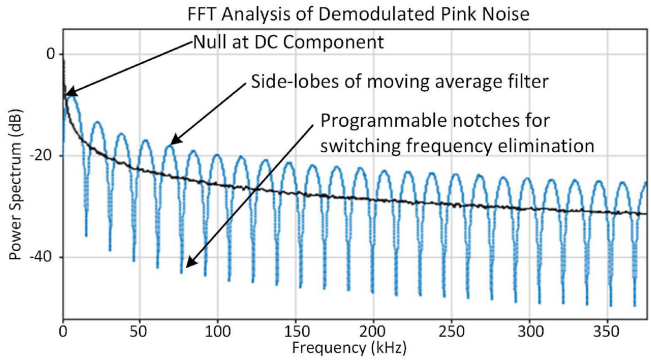

Fig. 4. FFT plot of pink noise with the time-shifted subtraction operation.

background noise. To extract the pink noise feature of the arc fault, the use of an autocorrelation function is proposed. The autocorrelation function is a measure of correlation between a signal and a delayed copy of itself, given by the following:

$$r(\tau) = E[x(\tau)\, x(t+\tau)] = \text{acf}(x(\tau)) \tag{3}$$

where $r(\tau)$ is the autocorrelation function of the measured time series $x(\tau)$, τ is the lag, $E[\cdot]$ is the expected value operator, and $\text{acf}(\cdot)$ is the short-hand notation for the autocorrelation function. When $r(\tau)$ is nonzero for any lag $\tau > 0$, the delayed copy at lag τ contains a degree of correlation.

In Fig. 7, a correlogram showing the magnitude of the autocorrelation coefficient as a function of lag is given for different colored noises. Colored noise is a term for PSD that follow the power law given in the following:

$$S(f) \propto \frac{1}{f^{\beta}} \tag{4}$$

where the function $S(f)$ is the magnitude of the PSD as a function of the frequency, f, and β is the exponential factor of the power law.

White noise ($\beta = 0$) is the typical baseline noise seen in many electrical systems and is characterized as a flat PSD with equal energy across all frequencies. White noise does not have any self-similarity or memory associated between consecutive time samples. Therefore, the autocorrelation coefficient is close to zero, as seen in Fig. 7 (black). Brown noise ($\beta = 2$) is the integration of white noise and contains strong correlations to previous values. If the lag index aligns with the switching frequency, $\tau = \Delta t_{\text{opt}}$, the delayed copies are in phase and completely correlated. Therefore, the autocorrelation coefficients will remain near 1, indicating strong self-similarity and correlation, as seen in Fig. 7 (blue).

Pink noise ($\beta = 1$), is a special case between white noise and brown noise showing some level of self-similarity but not completely. Therefore, as seen in Fig. 7 (red), the autocorrelation

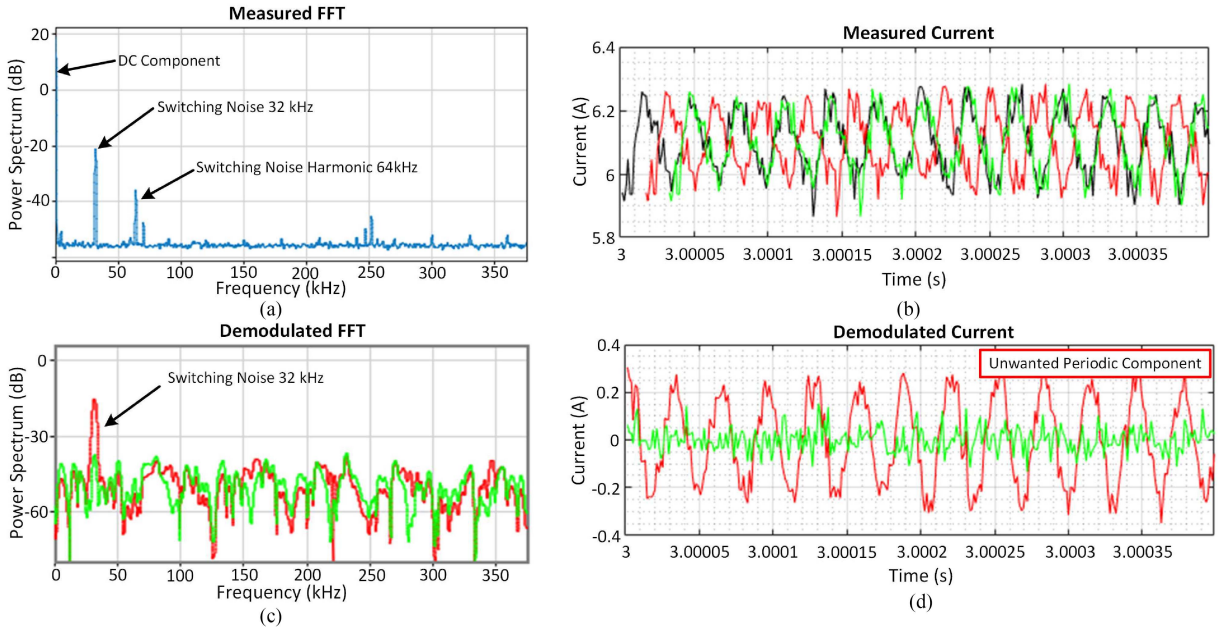

Fig. 5. (a) FFT analysis of PV current with switching noise. (b) Measured PV current (black), nonoptimal time-shifted current (red) and optimal time-shifted current (green). (c) Demodulated current FFT analysis. (d) Worst-case demodulated current scenario with a time-shift $\Delta t = \Delta t_{\text{opt}}/2$ doubling the amplitude of the periodic signal (red), optimal time-shift cancelling the amplitude (green).

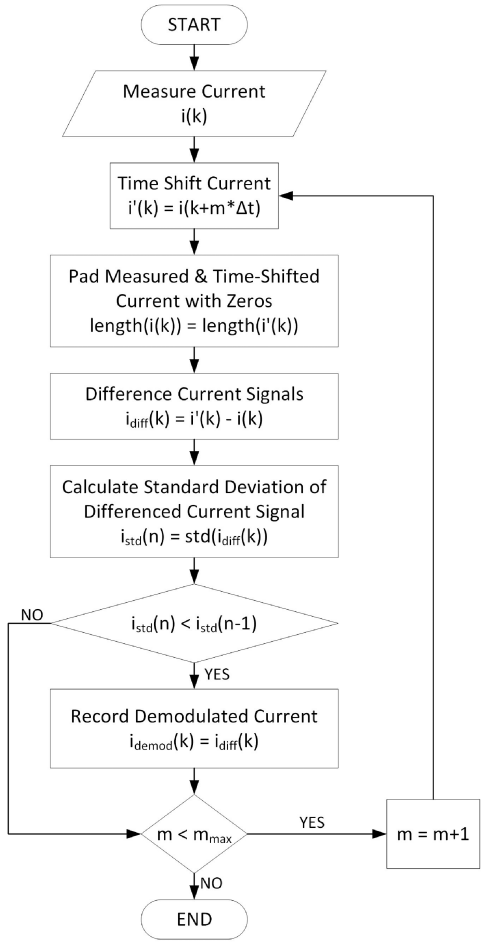

Fig. 6. Current demodulation algorithm flow diagram.

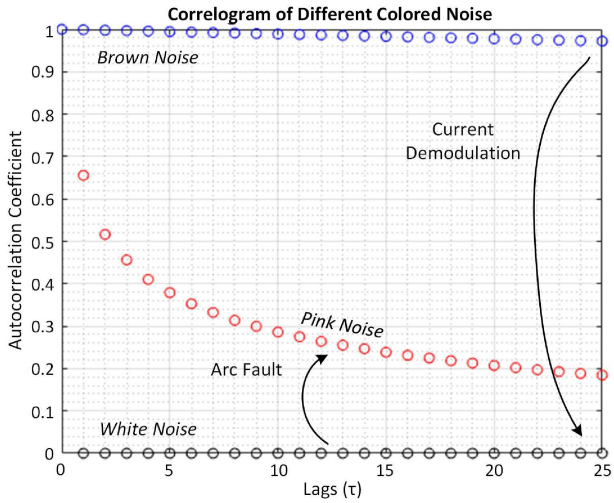

Fig. 7. Correlogram displaying the magnitude of the autocorrelation coefficient as a function of the lag for different colored noise: white (black), pink (red), brown (blue).

coefficients decrease from 1 slowly as the lag increases and the samples are removed further from the original value.

When large periodic noise that may cause false alarms or mask the arc fault signal is present on the measured PV current signal, then a large autocorrelation coefficient across multiple lags can be expected, similar to brown noise, $r(\tau) \approx 1$. However, once the current demodulation operation is completed, the periodic noise is eliminated and the background noise drops to an uncorrelated white noise baseline, $r(\tau) \approx 0$. If an arc fault is present, then the chaotic nature of the arc fault is not filtered through current demodulation and the autocorrelation coefficients will be

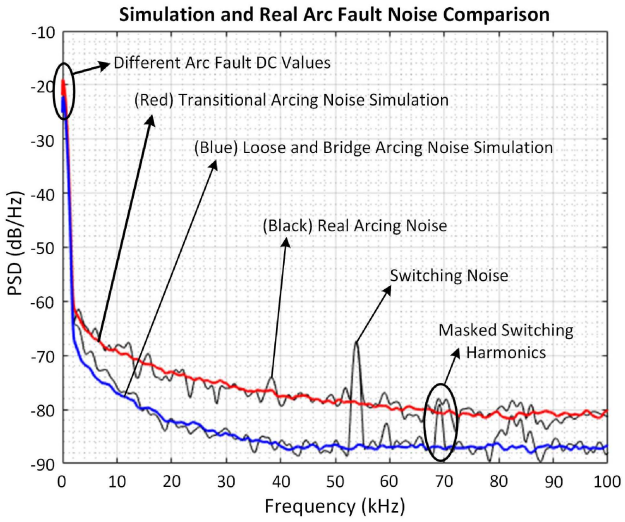

Fig. 8. Different arc fault states burning in air: loose and bridged arcing (blue); transitional arcing (red); and real arcing data (black).

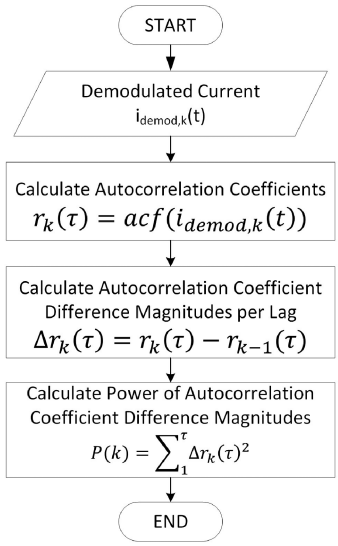

Fig. 9. Flow diagram of the calculation of the power signal for differenced autocorrelation coefficients.

some nonzero value with decreasing magnitude with increasing lag, $r(\tau) \neq 0$.

E. Differenced Autocorrelation Pink Noise Detector

An arc fault is an event that changes with the environmental conditions. Depending on the burning state of the arc fault, the noise injected into the system will change [30]. Therefore, when the arc fault is initiated, the autocorrelation coefficient of the current demodulated signal will show an initial jump from $r(\tau) \approx 0$ to $r(\tau) \neq 0$. However, as the arc fault continues to burn in air the arcing state changes, injecting different levels of pink noise to the PV current as shown in Fig. 8. When the arc fault is stable with no fluctuations in the arcing column between the electrodes [31], the arc fault is in either a loose or bridged arcing state with a smaller injection of pink noise. However, when the arcing column is sporadic and in between two stable states, the amount of pink noise injected increases because the arc fault impedance changes with arc length in the arcing column as it fluctuates over time [28], [30], [32].

The variation in the pink noise is quantified by subtracting the previous autocorrelation coefficient calculation from the present measured current window, generating a differenced autocorrelation coefficient parameter, as shown in the following:

$$\Delta r_k(\tau) = r_k(\tau) - r_{k-1}(\tau) \tag{5}$$

where $\Delta r_k(\tau)$ is the differenced autocorrelation coefficient between two demodulated current windows, k and $k-1$, as a function of lag, τ. The squared summation of the differenced autocorrelation coefficients across lag produces a power signal that quantifies the level of pink noise added to the system as given in the following:

$$P(k) = \sum_1^\tau \Delta r_k(\tau)^2 \tag{6}$$

where $P(k)$ is the power signal of the differenced autocorrelation coefficients calculated at the measurement window, k. A flow diagram of the calculation of the power signal for the differenced autocorrelation coefficients is given in Fig. 9. The power signal, $P(k)$, is averaged over a fixed time frame, k_0, as given in the following:

$$P_{\text{avg}}(n) = \frac{\sum_{k-k_0}^{k} P(k)}{k_0}. \tag{7}$$

For example, the power signal at $k = 20$ is averaged over a fixed time frame of $k_0 = 20$ ($k = 1$ *to* $k = 20$) to produce a single averaged power point with index $n = 1$. $n = 2$ would be the next averaged power point for the next time frame ($k = 21$ to $k = 40$). Therefore, k is the index of the measurement windows, and n is the index of the averaged power signals.

In Fig. 10, the power signal calculation is visualized for an arc fault ignition event. In Fig. 10(a), the current demodulated signal of five consecutive PV current measurements, $1 \leq k \leq 5$, is given, each represented with a different color. The measurement must be large enough to contain enough samples for the switching frequency, but small enough to not include low-frequency dc trends. Therefore, a measurement window of 0.5 ms is chosen to include all switching frequencies above 2 kHz.

Before the ignition of the arc fault, $k = 1$ (orange), the waveform shows no variations and remains relatively constant. When the arc fault is initiated between $k = 2$ (yellow) and $k = 3$ (purple), the current demodulated signal shows an increase in variation, indicating the presence of additional noise. When the arc fault stabilizes and the gap distance no longer changes, $k = 5$ (blue) the fluctuation in the demodulated current signal reduces, but still exists.

The autocorrelation coefficients reflect only the presence of uncorrelated white noise associated with the PV system before the arc fault, as shown in Fig. 10(b) (orange). After the ignition of the arc fault, the autocorrelation values decrease as a function

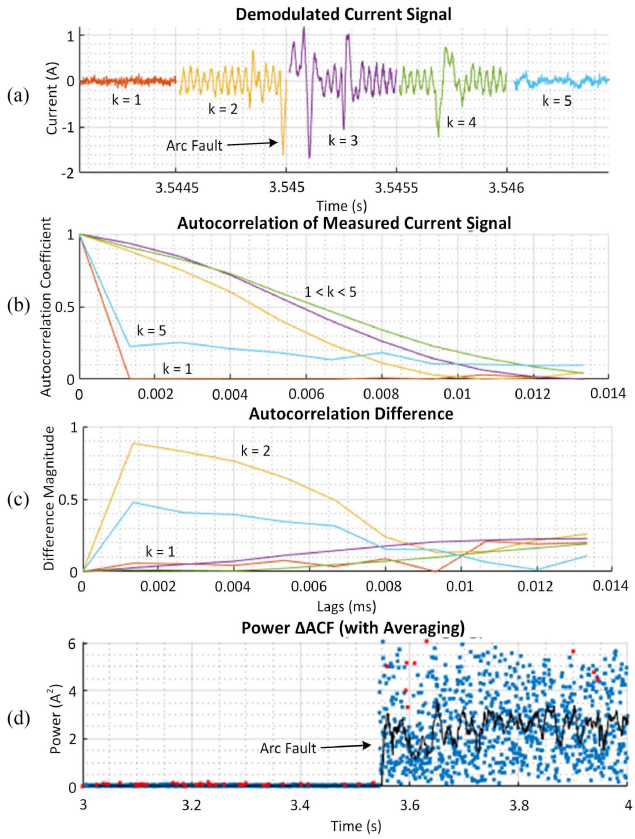

Fig. 10. (a) Five consecutive demodulated current signals. (b) Autocorrelation coefficient calculations of each measurement window. (c) Differenced autocorrelation coefficients for each corresponding measurement window. (d) Power signal of differenced autocorrelation coefficients.

of lag and show nonzero values, $r(\tau) \neq 0$. After the arc fault stabilizes, $k = 5$, the autocorrelation coefficients remain nonzero, suggesting the presence of self-similarity characteristic of an arc fault in the PV system.

In Fig. 10(c), the differenced autocorrelation coefficients for each corresponding measurement window are calculated according to (5). The increased autocorrelation coefficients at the arc fault ignition results in a large differenced autocorrelation coefficient. While the arc fault is burning, the difference between autocorrelation coefficients is smaller than ignition, but remains nonzero because the intensity of pink noise changes. In Fig. 10(d), the power signal for differenced autocorrelation coefficients for 1 second is shown and the average power signal increases from $P_{\text{avg}}(n) \approx 0$ to $P_{avg}(n) \gg 0$ at the ignition of the arc fault. Therefore, the power signal of the differenced autocorrelation coefficients can detect the presence of pink noise.

F. Outlier Elimination

The ignition of the arc fault generates a sudden decrease in the current magnitude because of the added impedance of the arc fault in the PV system [11], [18], [30]. However, other cd disturbances occur which also cause sudden changes in the current signal, such as dc disconnect switch operations, sudden partial shading, irradiance changes, and load changes. Therefore,

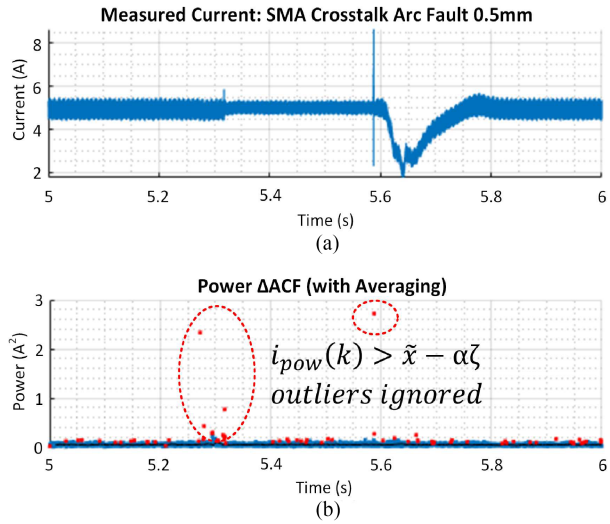

Fig. 11. (a) Monitored PV string current with arc fault occurring elsewhere in the PV array on a parallel PV string. (b) Outliers marked in red by the Hampel identifier and ignored for future calculations.

outlier elimination is necessary to remove single transient events while allowing continuous transients like arc faults to pass through.

In [33], four outlier detection rules are explored for PV fault detection, which are as follows:

1) the 3σ rule;
2) the standard Boxplot outlier rule;
3) the Hampel identifier;
4) local outlier factor.

The Hampel identifier has low complexity and is resistant to large contamination levels and is chosen for the outlier detection rule. The contamination level is defined as the fraction of outliers to a given data set as shown in the following:

$$\text{contamination level} = \frac{\text{number of outliers}}{\text{total number of samples}}. \quad (8)$$

The Hampel identifier breaks down at contamination levels greater than 50% compared to the 10% or 25% in the 3σ and boxplot outlier rules, respectively. According to the Hampel identifier, an outlier is defined as in the following:

$$|x_i - \tilde{x}| > \alpha\zeta \quad (9)$$

where x_i is the potential outlier sample observed, $\tilde{x}$ is the sample mean, α is the threshold parameter, usually set to 3, and ζ is the measure of variation as defined below for the Hampel identifier in the following:

$$\zeta = \frac{1}{0.6745} \text{ median } \{|x_i - \tilde{x}|\}. \quad (10)$$

For example, in Fig. 11(a), crosstalk between parallel PV strings may incorrectly trip a monitored PV string. When an arc fault occurs elsewhere the transient is coupled onto a parallel PV string. The Hampel identifier recognizes the transient events and properly eliminates them in Fig. 11(b). However, in Fig. 10(d), the arc fault is continuous and the sudden increase in the power signal is not recognized as outliers.

III. Arc Fault Detection Criteria

The arc fault is a continuous event that injects a pink noise frequency spectrum on the PSD. Therefore, two energy signals are generated from the power signal of the differenced autocorrelation coefficients to measure the persistent presence of arc fault noise and variations in the injected arc fault noise over time. The energy signals are compared against simple threshold violation criteria to determine the presence of an arc fault.

A. Arc Fault Energy Signals

The energy of the power signal is the measure of the difference in the self-similarity injected by the arc fault over a fixed time period (a group of time frames), n_0, of the averaged power signals shown in the following:

$$G(n) = \sum_{n-n_0}^{n} P_{\text{avg}}(n). \tag{11}$$

Therefore, if the arc fault continues to burn, pink noise is continually present on the current. The average power signal of the differenced autocorrelation coefficient remains high and the summation over time presents a gradual increase in the energy signal.

The second energy signal is a measure of the variation in the power signal over time to represent the persistent presence of a variable impedance added by the arc fault. The standard deviation of the power signal, $P_{\text{std}}(n)$, is calculated using the previous k_0 samples used to measure the average of the power signal as shown in the following:

$$P_{\text{std}}(n) = \text{std}(P(k-k_0:k)). \tag{12}$$

When the standard deviation of the power signal is summed over the given time period, n_0, the energy of the variation of pink noise, $G_{std}(n)$, injected to the PV system can be measured as shown in the following:

$$G_{\text{std}}(n) = \sum_{n-n_0}^{n} P_{\text{std}}(n). \tag{13}$$

Therefore, the two energy signals, $G(n)$ and $G_{\text{std}}(n)$, represent the persistent arc fault frequency spectrum and random variation of the injected pink noise as a function of the arcing state, respectively.

B. Arc Fault Detection Criteria

When both energy signals calculated in (11) and (13) cross their respective energy thresholds, G_{thresh} and $G_{\text{std,thresh}}$, an arc fault is declared, as shown in the following:

$$\text{Detection Criteria 1}: \; G(n) > G_{\text{thresh}} \tag{14}$$

$$\text{Detection Criteria 2}: \; G_{\text{std}}(n) > G_{\text{std,thresh}}. \tag{15}$$

The thresholds are determined to detect the arc within the specified time constraint given by the UL 1699B standard shown in the following [35]:

$$t_{\text{arc}} = \min\left\{\frac{750J}{V_{\text{arc}} I_{\text{arc}}}, 2.5\text{ s}\right\} \tag{16}$$

where t_{arc} is the maximum time allowed for arc fault detection, V_{arc} is the voltage across the arc fault, and I_{arc} is the current across the arc fault.

C. Arc Fault Detection Implementation

The constraints of the presented algorithm stem from the practical constraints of the digital-to-analog converter (DAC) and digital signal processor (DSP) in accurately sampling the requisite number of data points to replicate a periodic signal. For instance, considering a data acquisition rate of 1 Msa/s and a minimum of 10 points needed to reconstruct a 100 kHz sine wave, this falls within the capability of numerous DACs and DSPs.

DWT is frequently acknowledged for its effectiveness in signal conditioning. The computational complexity of DWT with a sample length of N is denoted as $C(N)$, where $C(\cdot)$ represents the number of computations. FFT, another widely employed technique, is estimated to involve $C(N\log(N))$ computations. Similarly, autocorrelation calculations also entail $C(N\log(N))$ computations. However, the proposed algorithm does not necessitate calculations for all lags from 0 to N–1. Consequently, it demonstrates faster processing than FFT and can compete effectively with DWT. Table I presents a comparative overview of various attributes of the proposed algorithm in contrast to other state-of-the-art arc fault detection methods.

IV. Experimental Results

The current demodulation operation and pink noise extraction of arc fault noise is validated using the experimental data from a 1.2 kW off-grid and 3.9 kW grid-tied PV system. Different string inverters with different MPPT and switching frequency operations have been tested without changing the signal conditioning parameters and detection thresholds of the arc fault detection algorithm proving versatility of the algorithm in different PV environments. False alarms from unwanted tripping conditions have also been distinguished from arc fault conditions and avoided.

A. Arc Fault Detection in Off-Grid PV Systems

An arc fault is generated in an off-grid PV system as shown in Fig. 12(a). The switching frequency of the inverter and the charge-controller of the off-grid PV system is similar to the background noise and can be seen as negligible as seen in the persistence spectrum in Fig. 12(b). The persistence spectrum shows the frequency on the y-axis with respect to time on the x-axis and the magnitude of the power spectral density of the frequency coefficients is given relative to the lowest value (blue) to the highest value (yellow). After the current waveform has been demodulated, in Fig. 12(c), the dc trend is eliminated and the signal is zero-meaned. The persistence spectrum reveals that the arc fault noise now dominates the spectrum (yellow) and is extracted from any other background noise.

In Fig. 13, the tracked inverter PWM switching frequency that is demodulated, defined as the shift coefficient, is given. However, because the noise from the switching frequency is

TABLE I
COMPARISON OF DETECTION METHODS

Detection Method	Advantages	Limitations	Computational Intensity	Detection Speed
Time-Domain Current Magnitude Changes [17], [28], [36]	- Easy implementation - Simple detection rules	- Misdetections from MPPT - Susceptible to low-frequency noise - Higher false positives/negatives	Light	Medium/Fast
Fast-Fourier Transform (FFT) [18], [37], [38], [39], [40]	- Simple detection rules - Widely implemented and studied	- Only frequency information available - May trip from inverter, converter, and controller noise - Limited frequency extraction of arc signal	Heavy	Slow
Short-Time Fourier Transform (STFT) [4], [41]	- Utilizes time- & frequency-domains	- Requires proper tuning of detection window length	Heavy	Slow
Discrete Wavelet Transforms (DWT) & Wavelet Decomposition Packets (WPD) [17], [18], [29], [42], [43], [44], [45], [46]	- Widely studied - Utilize time & frequency-domains - Current discontinuity detection - Robust against false negatives - Multilayer time-frequency characterization of arc faults	- May trip from inverter, converter, and controller noise - Requires proper tuning of decomposition levels - Can not distinguish from increased white noise floor	Medium	Slow/Medium
Statistics Based [10], [18], [19], [20], [21], [30], [47], [48], [49]	- Easy implementation - Can be used with current and voltage signals - Observes the increased entropy/chaotic/random nature of arc faults	- Precise thresholds required - Precise tuning of FIR filters - Usually pairs with other detection methods - Highly susceptible to false positives from environmental conditions, PV control algorithms, and DC magnitude changes	Light/Medium	Depends
Machine-Learning [22], [24], [25], [26], [50], [51], [52]	- Effectively differentiate arc fault transient behavior - Adaptable across broad spectrum of applications - High accuracy for known arc fault conditions	- Requires large training data sets - Accurate modeling of arc faults is required - Highly complex implementation - Susceptible to overfitting - Requires prior knowledge of PV conditions and arc faults	Heavy	Fast
Spread-Spectrum Time-Domain Reflectometry (SSTDR) [53]	- Can be completed offline - Predictive fault detection	- High sampling rates - Inverter and converter noise causes false positives - Requires prior knowledge of healthy PV conditions	Heavy	Unknown
Current Demodulation and Autocorrelation Coefficients (proposed algorithm) [11], [26]	- Doesn't require prior knowledge of PV system - Implemented on wide-range of PV system power levels - Robust against DC current magnitude changes - Robust against transient conditions - Observes pink noise characteristic of arc faults	- High sampling rates - Tuning of detection criteria thresholds - Susceptible to false positives from other pink noise sources	Medium	Medium/Fast

negligible in this particular off-grid system, the demodulation algorithm will choose a time-shift or shift coefficient that minimizes the standard deviation of the current signal and detrends the DC trend of the data without any particular elimination of higher periodic noise.

In Fig. 14, the power signal and energy signal calculations are shown for the off-grid PV arc fault. In Fig. 14(a), the power signal of the differenced autocorrelation coefficients begins to increase after the arc fault is initiated. Therefore, the energy signal begins to slowly rise in Fig. 14(b). The arc fault continues to burn through the electrodes causing more variation in the injected pink noise signature of arc faults. Therefore, the autocorrelation coefficients are no longer constant and have large variations as shown in the increase in standard deviation in Fig. 14(c). As the arc fault continues to burn the energy of the standard deviation will continue to rise as shown in Fig. 14(d). Therefore, PV current signals without a large switching frequency component can still be "demodulated" using the current demodulation operation and the pink noise signature can be isolated and extracted using the differenced autocorrelation coefficients.

B. Arc Fault Detection in Grid-Tied PV System (Inverter A)

In Fig. 15(a), an arc fault is generated in a 6 × 2 PV configuration (six modules in series, two strings in parallel) using Inverter A. The actual switching frequency of Inverter A is approximately 20 kHz which the current demodulation operation tracks successfully as shown in Fig. 15(b). The demodulated current eliminates the low-frequency dc trends and generates a zero-meaned signal while preserving the arc fault frequency noise as seen in Fig. 15(c). The arc fault detected signal is given in Fig. 15(d).

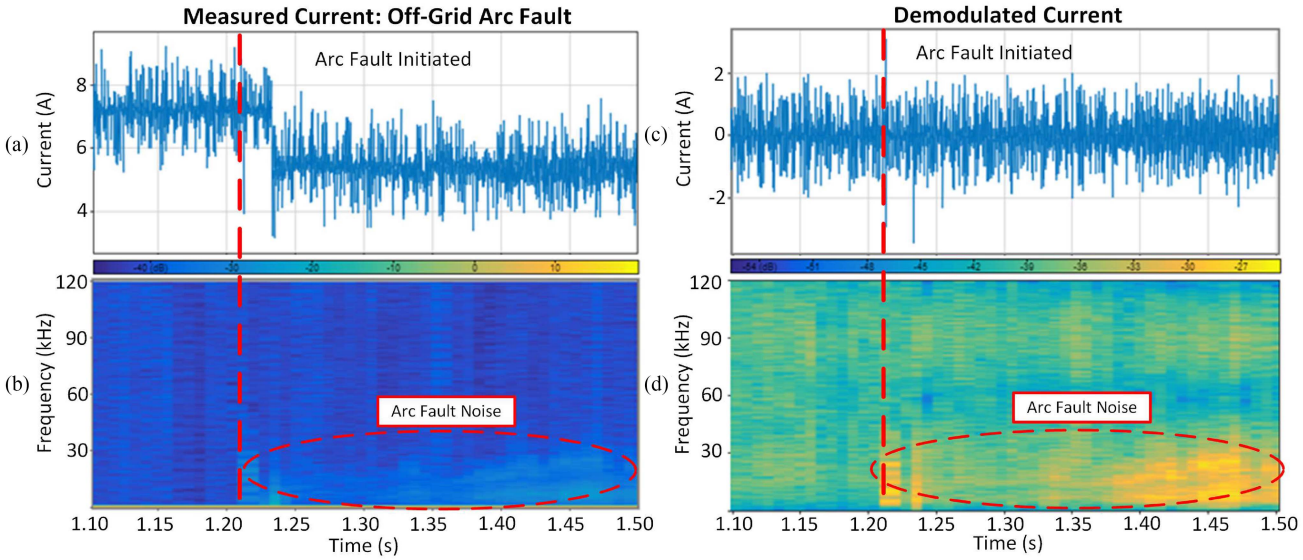

Fig. 12. (a) Measured off-grid current with an arc fault. (b) Persistence spectrum of measured PV current. (c) Demodulated current signal with an arc fault. (d) Persistence spectrum of demodulated current signal.

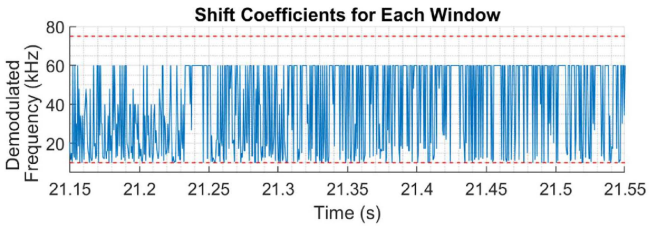

Fig. 13. Shift coefficient of the off-grid PV system.

The individual analysis of all the energy signals for the test in Fig. 15 is given in Fig. 16. In Fig. 16(a), at the ignition of the arc fault, the power signal is seen to increase immediately. Therefore, the corresponding energy signal begins to slowly increase as seen in Fig. 16(b). In Fig. 16(c), the arc fault continues to burn and the magnitude of injected arc fault noise changes over time, resulting in an increase in the standard deviation of the power signal. The corresponding energy signal increases as seen in Fig. 16(d). Therefore, when both energy signals have crossed their respective thresholds an arc fault is detected as seen in Fig. 15(d).

C. Other PV Configurations With Arc Fault

In Fig. 17, arc faults are generated in five different inverters, each with a different PV configuration. Inverter A and Inverter B are the string inverters tested at Northeastern University, as shown in the experimental setup in Fig. 3. The arc fault generated on Inverter C is data from a 3-phase inverter tested by Sandia National Laboratories [6], [15]. The specific PV configuration and specification of the inverter is unknown. Therefore, the proposed current demodulation and pink noise extraction algorithm can be tested for robustness against unknown parameters. The arc fault is generated at time $t = 0$ s for all inverter and PV configurations.

In Fig. 17(a), the power signal of the differenced autocorrelation coefficients is given. Arc faults generated on Inverter A and Inverter B with both the 6×2 and 12×1 PV configurations (red, blue, green, pink) all show an increase in the power signal at time $t = 0$ s. The arc fault generated in a PV system with the 3-phase Inverter C also shows an increase in the magnitude of the power signal. Therefore, the energy signal of the differenced autocorrelation coefficients calculated from the magnitude of the power signal also increase as shown in Fig. 17(b).

In Fig. 17(c), the standard deviation of the power signal is given. All five arc fault cases (6×2 Inverter A, 12×1 Inverter A, 6×2 Inverter B, 12×1 Inverter B, 3-Phase Inverter C) show an increase in standard deviation of the power signal because the arc fault injects a different magnitude of pink noise as it burns in air. In Fig. 17(d), the energy signal of the standard deviation of the power signal increases for all five arc fault cases.

D. Arc Fault Detection Time

By the UL1699B standard as shown in (16), the maximum detection time is the minimum between 2.5 s and the time calculated using the arc fault energy [36]. In Fig. 18, trip times for the arc faults generated in the different PV configurations. For example, in the worst-case scenario, the 12×1 PV configuration with Inverter A generates an arc fault with an arcing current of approximately 5 A with an arc fault voltage drop of 50 V. According to (16), the detection time is calculated to be $t_{\text{arc}} = \min\left\{\frac{750\ \text{J}}{(50\ \text{V})(5\ \text{A})}, 2.5\ \text{s}\right\} = 2.5$ s. Although the objective of the AFD algorithm was only to satisfy UL1699B detection times, the proposed algorithm demonstrated the trip time of 120 ms, which is an order of magnitude faster than required. In fact, the 120 ms trip time would have even satisfied UL requirements for an arc fault power as high as 6.25 kW, which is not possible in a maximum PV system power of 3 kW. In addition, the UL 1699B standard requires tests for arc faults up to a power

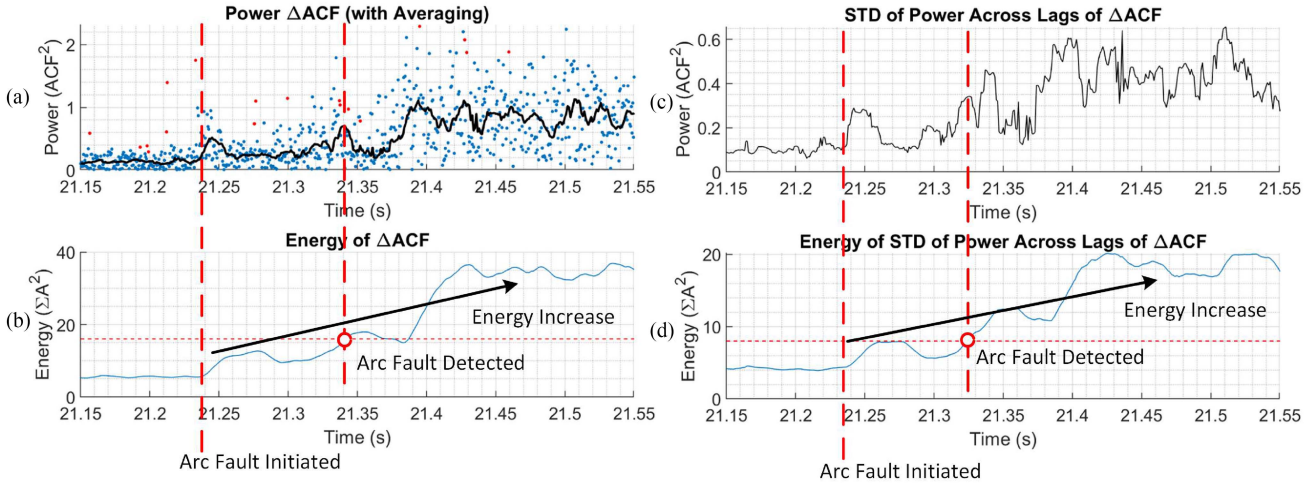

Fig. 14. (a) Power signal of differenced autocorrelation coefficients. (b) Energy signal of power of signal. (c) Standard deviation of power signal. (d) Energy signal of standard deviation of power signal.

of 300 W. Therefore, all potential arc fault cases for this PV configuration could be detected.

In the real 6×2 PV configuration with Inverter A and Inverter B have an arc fault detection time of approximately 10 ms. The 12×1 PV configuration for Inverter A has a detection time around 120 ms and the 12×1 PV configuration for Inverter B has a detection time around 44 ms. Lastly, the PV configuration with the 3-phase Inverter C has a detection time of approximately 19 ms. These detection times are all well within the 2.5 s maximum for these low power arc faults.

It is interesting to notice that the 12×1 PV configuration has almost an order of magnitude longer detection time by than that of the 6×2 PV configuration. The 12×1 PV configuration (blue, pink) has a larger open-circuit, V_{oc}, and maximum power point (MPP) voltage, V_{mpp}, than that of the 6×2 PV configuration (red, green). The arc fault is monitored on each PV string and the measured current (on each individual PV string) is the same, regardless of the number of PV modules in series. The voltage across the arc fault generated by the PV string with higher, V_{oc} will have a larger arc fault voltage drop because of the larger voltage source. The larger arc fault voltage drop generates a "more stable" arc, which is analogous to tighter arc column [30], [31]. Therefore, the arc fault injects a smaller magnitude of pink noise and generates less fluctuations in the impedance [30], [31], as shown in Fig. 17(a) and (c). The smaller power signal magnitude decreases the slope of the energy signal, and the energy rises slower as shown in Fig. 17(b) and (d). The detection times are longer because the energy signals cross the detection threshold after a longer period. However, it is still within the 2.5 s maximum detection threshold.

Therefore, the detection values mainly depend on: 1) the signal integrity which may generate low signal-to-noise ratios (SNR) decreasing the effectivity of the differenced autocorrelation coefficients and 2) voltage of the PV string which determines the stability of the arc fault, decreasing the amount of pink noise available for detection. Unwanted tripping tests that support these claims are given in the next section.

String inverters typically range from a few hundreds of watts to a few kilowatts with short circuit ratings for each string near 10 A. The exact values of the detection thresholds in the proposed algorithm were determined from a collection of real arc fault data from two string inverters, an off-grid inverter, and 3-phase inverter at system power levels up 3 kW with varying arc fault lengths from 0.5 to 5 mm. For robustness, the value for the thresholds in (14) and (15) in a particular PV system can be generally determined by looking at the energy levels in (11) and (13) in a normal system and setting thresholds around one order of magnitude greater, depending on the desired speed for detection. The SNR of the detectors should be below +3 dB (or twice the signal power) such that the arc fault information can be extracted effectively.

Of the two commercial standalone AFDD tested shown in Fig. 3, Commercial AFDD A was unable to detect smaller energy arcs under 300 W with low SNR and the "stable" arcs generated by the 12×1 PV configuration.

In total, 285 arc faults were generated under various weather conditions ranging from partly cloudy and sunny weather between the months of July and November. The algorithm is specifically tuned for the wide range of cases mentioned and can detect 97.6% of all arc fault cases. The 2.4% missed detections are generated from intermittent arc faults where the arc fault generator stalls, instantly closing the arc fault gap after attempting to separate. Despite these instances going unnoticed, the arc fault is not sustained and not subject to the UL1699B detection criteria. Consequently, the proposed algorithm complies with UL requirements with 100% accuracy rate.

V. Unwanted Tripping Conditions

This section demonstrates that the proposed AFD algorithm does trigger false alarms when tested with the three unwanted tripping loading conditions as outlined UL 1699B standard including the following:

1) inverters, converters, and charge controllers;

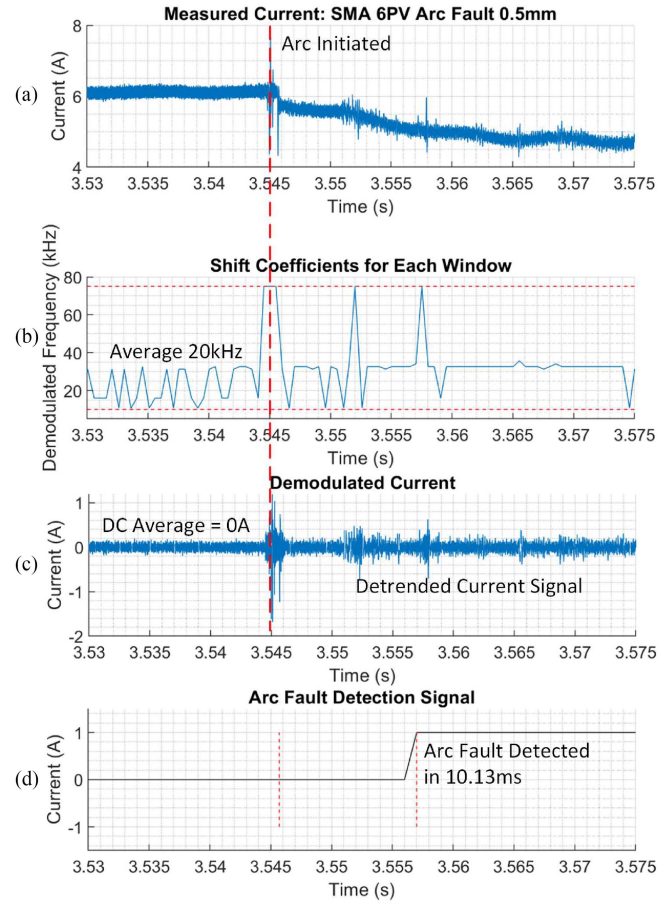

Fig. 15. (a) Inverter A of grid-tied PV system with arc fault. (b) Time-shift coefficients averaging 20 kHz. (c) Demodulated current signal. (d) Arc fault detected.

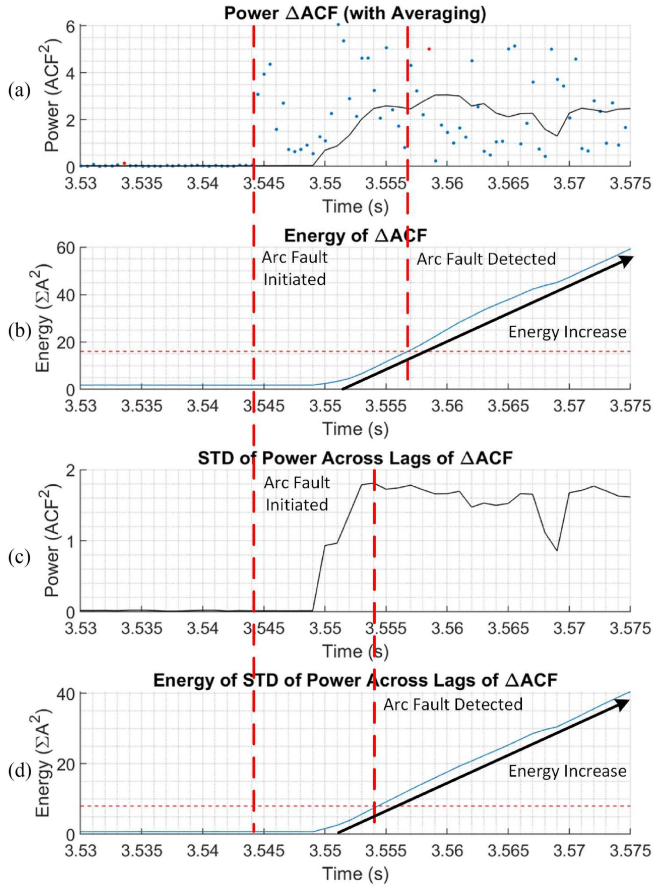

Fig. 16. For Inverter A with 6 × 2 PV system. (a) Power of differenced autocorrelation coefficients. (b) Energy of averaged power signal showing increase after arc fault. (c) Standard deviation of power signal. (d) Energy of the standard deviation of the power signal showing increase after arc fault.

2) dc switch operations and;

3) irradiance changes.

The UL 1699B also lists unwanted tripping tests listed for different PV configurations, such as module-level dc/dc converters and inverters to test the effect of switching frequencies and EMI noise [35]. Module-level PV configurations are not available in the experimental setup given in Fig. 3 and have been reserved for future research.

Moreover, this section showcases the resilience of the proposed algorithms through the incorporation of tests, including simultaneous multiple inverter operations, crosstalk between two PV strings, and start-up conditions, as illustrated in Fig. 17. The undesired tripping condition is initiated at $t = 0$ s, and it is noteworthy that none of these tests resulted in triggering an arc fault alarm.

A. *Loading Condition I—Inverters and Controller Noise*

In loading condition I, several different conditions are presented in the UL1699B standard. The PV array's dc power is either converted into ac power tied to a grid or into dc power through a charge controller, which is then tied to a battery bank as an off-grid system or goes through second stage to be tied into the grid. In this loading condition, the proposed algorithm should successfully avoid false positives from low-frequency current magnitude changes from the MPP and the high-frequency noise coming from the switching noise of the first stage (inverter tied to a grid or the charge-controller tied to the battery bank).

Illustrated in Fig. 7, brown noise, encompassing the distinct switching noise generated by inverters and converters, undergoes current demodulation in (1) to be transformed into white noise. Following this transformation, white noise, when subjected to the differenced autocorrelation pink noise detector outlined in (5) and (6), is not classified as arc fault noise. Inverter A and Inverter B have different switching frequencies, 20 and 32 kHz, respectively, while the switching frequency of the 3-phase Inverter C is unknown. During the steady-state of Inverter A, Inverter B and the 3-phase Inverter C ($t < 0$ s), all energy levels remain close to zero and do not meet the detection criteria given in (14) and (15). Therefore, even though different and unknown switching frequencies are in operation, the algorithm is successfully able to avoid false positives from inverter noise operating with MPP.

In addition, noise generated by a charge controller in an off-grid system as shown in Fig. 2(a) do not affect the efficacy of the proposed algorithm. The arc faults are successfully detected

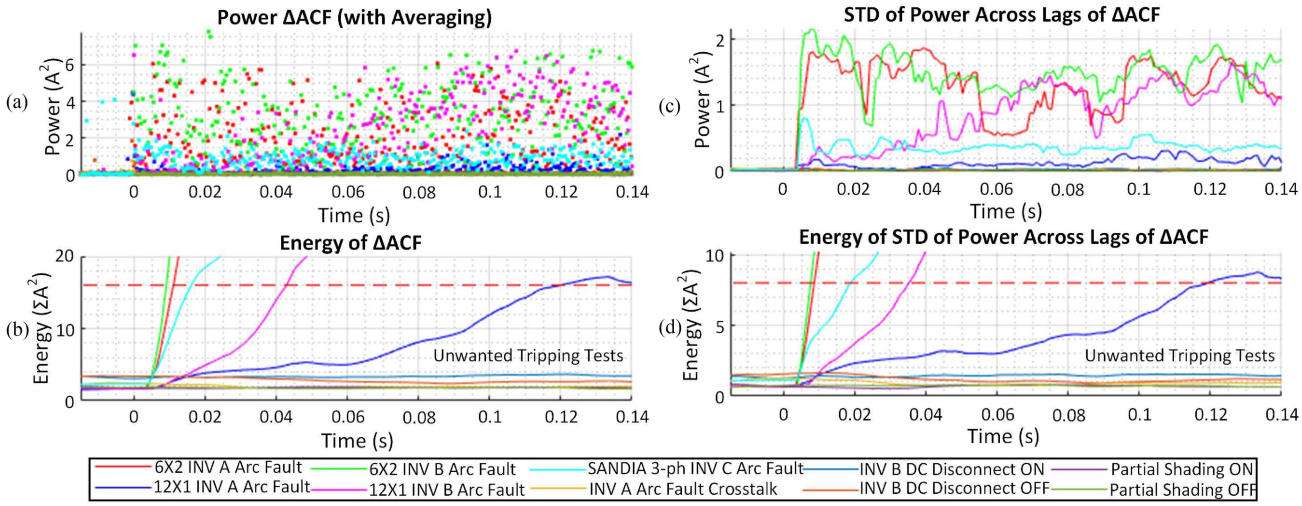

Fig. 17. Arc faults and unwanted tripping conditions generated on different inverter and PV configurations: (a) Power of differenced autocorrelation coefficients. (b) Energy of averaged power signal. (c) Standard deviation of power signal. (d) Energy of the standard deviation of the power signal.

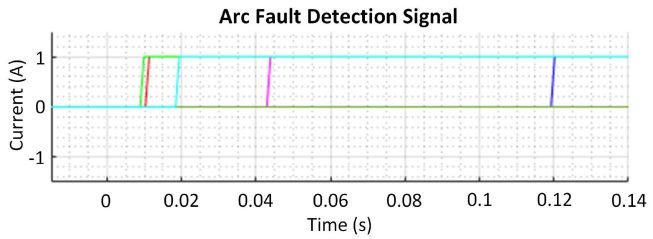

Fig. 18. Arc fault trip time for different arc fault and unwanted tripping tests (same legend as Fig. 17).

as shown in Fig. 12, while the charge controller noise before the arc fault is successfully ignored.

The inverter may also have different control schemes such as spread-spectrum/frequency jittering to reduce EMI and frequency shifting to accommodate a wide range of load levels. The proposed algorithm may have the potential to detect frequency drifts at rates longer than the measured time window of 0.5 ms given in Section II-E, which is chosen to include switching frequencies greater than 2 kHz. In Fig. 15(b), the measured switching frequency seems to shift, but the current demodulation searches for the optimal time shift per window, as shown in the algorithm presented in Fig. 6, Section II-C, successfully detecting a switching signal averaging 20 kHz over a long period of time. However, the effects of the hysteretic controllers, constant off time, and other variable switching frequency control schemes have not been fully tested and leaves room for future research.

B. Loading Condition II—DC Switch Operations

In loading condition II, the PV array configuration is changed by using a dc switch at the PV array to either connect or disconnect PV strings. For example, a 6×1 PV configuration would be changed to a 6×2 PV configuration by connecting a parallel PV string. The operating point of the PV array will suddenly change because of the addition or subtraction of a PV string which is essentially a current source. This is tested in this research by using the dc disconnect switch located before the fuses inside the junction box as shown in Fig. 3. The sudden current magnitude change should not cause false positives in the proposed algorithm.

However, the current demodulation scheme generates a null at dc frequencies eliminating false positives from sudden magnitude changes. In addition, the color of the injected noise does not change and the exponent of the power law in (4) remains as white noise ($\beta = 0$). Therefore, the standard deviation of the power signal of the differenced autocorrelation coefficients does not change, as shown in Fig. 17(d) and the energy levels do not meet the detection criteria set by (14) and (15). Therefore, when a PV string is suddenly added to/subtracted from the overall system, the magnitude of the energy signal does not increase or spike at the initiation of a dc switch operation as shown in Fig. 17(b) and false positives are successfully avoided.

C. Loading Condition III—Irradiance Step Changes

Lastly, loading condition III irradiance step changes from sudden partial shading such as cloudy weather, moving shadows from stationary objects such trees and chimneys as the sun passes overhead, and unexpected shadows such as people, animals, or small clouds moving overhead should not trick the proposed algorithm. These generate low-frequency current magnitude changes that should be successfully disregarded.

Partial shading ON and partial shading OFF are generated by quickly applying a blackout cloth over portions of the PV string being monitored. These test results are shown in Fig. 17. Like in Loading Condition II with dc switch operations, sudden irradiance changes generate a shift in the current magnitude which are nulled by the current demodulation scheme. In addition, only white noise exists in the system with no additional injected color

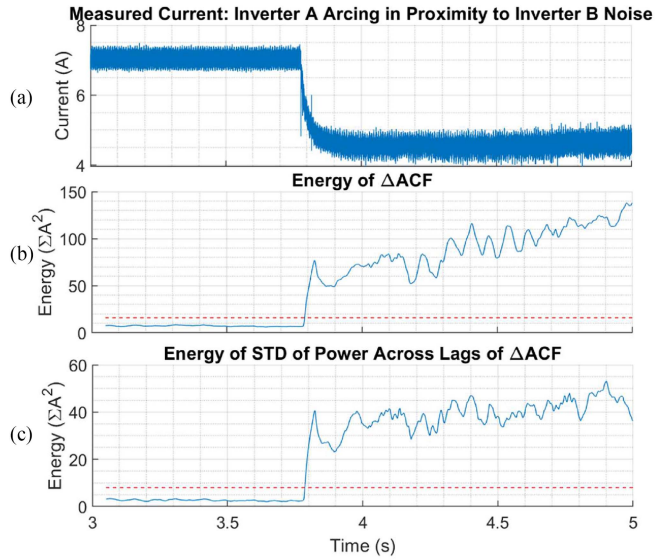

Fig. 19. Arc fault detection on Inverter A with Inverter B noise coupled on the ac grid in close proximity.

noise. The detection criteria are not met in (14) and (15), and the false positive from irradiance step changes are successfully avoided, as shown in Fig. 18.

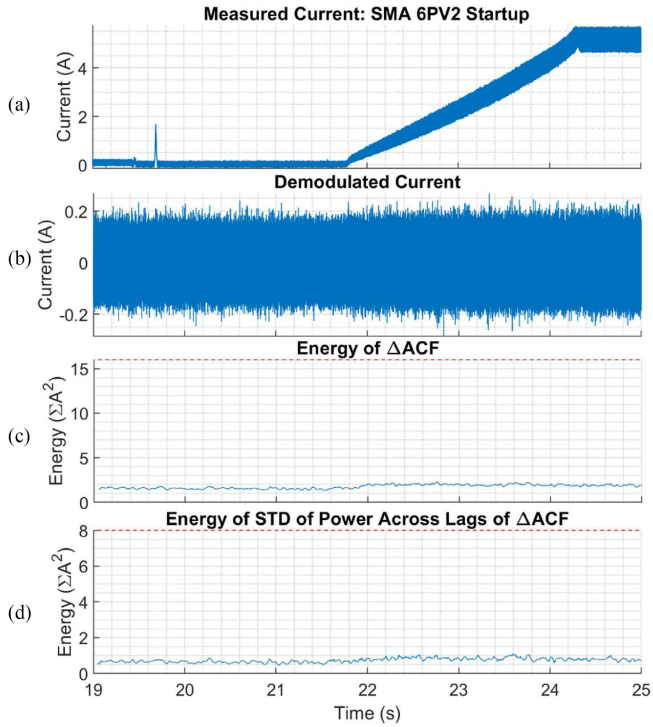

Fig. 20. Startup of Inverter A.

D. Additional Loading Conditions—Simultaneous Operation, Crosstalk, Inverter Start-Up, and PV System Degradation

Because of the nature of the experimental setup in Fig. 3, Inverter A and Inverter B are connected to each other at a combiner box before being injected to the ac grid source. Therefore, ac noise generated by one inverter may couple to the second inverter. In a specific trial, both Inverter A and Inverter B operate concurrently, each with a 6 × 1 PV configuration operating at MPP and delivering approximately 1.5 kW. In Fig. 19(a), before the arc fault is generated at 3.78 s, any noise generated by Inverter B is successfully filtered and disregarded. The detection criteria in (14) and (15) are not satisfied, as shown in Fig. 19(b) and (c), respectively. However, the pink noise of a 120 W arc fault is detected and both criteria (14) and (15) are met within 15 ms of ignition. Therefore, any noise transmitted from a parallel inverter operating at the same ac node inside the combiner box is successfully isolated, preventing false positives, while simultaneously detecting low-power arc faults generated with arcing gaps of less than 0.5 mm.

When an arc fault occurs on a PV string parallel to the monitored PV string, crosstalk between parallel PV strings has shown to trip the AFDD (specifically Commercial AFDD B) on the monitored "good" PV string. As shown in Fig. 11(a), the arc fault occurs around $t = 5.3$ s. However, using the proposed current demodulation algorithm, the monitored string recognizes a transient event from the burst of energy of the arc fault on a parallel string but is successfully ignored as an outlier in Fig. 11(b). The system begins to retrack the MPP between $t = 5.3$ s and $t = 5.8$ s. However, the monitored "good" string does not generate false positives from arc faults generated on a different string. Therefore, the proposed arc fault algorithm successfully isolates arc fault events transpiring on its respective monitored PV string while disregarding noise originating elsewhere in the system.

The start-up condition of Inverter A, shown in Fig. 20(a) was observed to trip Commercial AFDD B. However, the proposed current demodulation scheme eliminates the transient from turning ON the dc switch to Inverter A at 19.65 s and the dc trend from MPP initiated between 21.80 and 24.40 s, as shown in Fig. 20(b). The energy levels for the detection criteria in (14) and (15) are not met as shown in Fig. 20(c) and (d), respectively. Therefore, the proposed algorithm successfully ignores the start-up condition that may cause false positives in Commercial AFDD B.

E. PV Degradation and Sensor Inaccuracy

Lastly, the effects of PV degradation due to aging and sensor inaccuracy is simulated using collected arc fault data. When a PV system ages, there can be degradation of solder joints which is simulated arc faults generated by submillimeter gaps as seen in the experiments of Sections IV and V-D. When a PV system degrades, the *I–V* curve changes, reducing the magnitude of current at the MPP. This is simulated on data collected from an arc fault generated on a 6 × 2 PV configuration shown in Fig. 21(a). Current demodulation generates a null at the dc frequency, thereby ignoring changes in the current magnitude. Therefore, there is no change in the energy of arc fault noise detected. In Fig. 21(b) and (c), the original energy values (blue) overlap with the reduced current magnitude values (blue).

However, as a PV system degrades, there may be a higher noise floor, which can also be similar to lower SNR in the

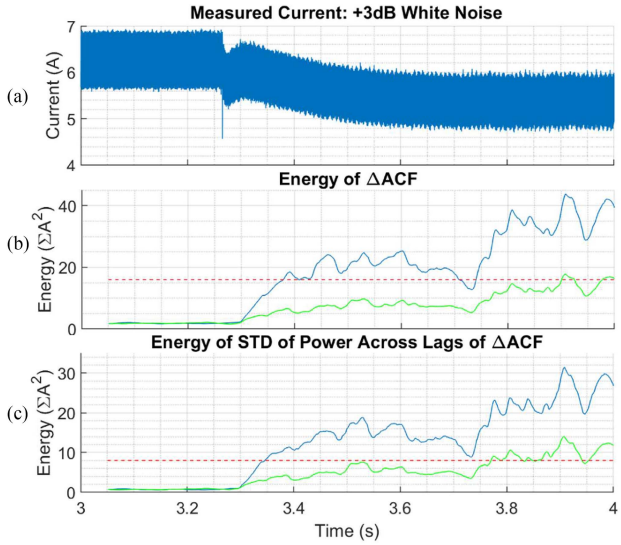

Fig. 21. Arc fault detection of original signal (blue) compared to signal with +3 dB added white noise (green).

current sensor. This is simulated by artificially adding +3 dB (which is a normalized power ratio of approximately 2 times the input signal) of white noise onto the original data collected in Fig. 21(a). In Fig. 21(b) and (c), the increased noise floor does reduce the magnitudes of the energy calculated from the differenced autocorrelation pink noise detector from (3) to (7). The detection time is increased from 12 to 65 ms. Therefore, although the algorithm demonstrates robustness to current sensor noise, it also indicates that even greater magnitudes of signal degradation, e.g., above twice the input power signal could increase detection times that eventually violate (16). In addition, dc biases that occur in the sensor are similar to the current magnitude changes observed from loading condition II and III and can be successfully disregarded.

Therefore, the proposed arc fault detection algorithm can successfully detect arc faults in a variety of PV configurations without false alarms from unwanted tripping conditions caused by the switching frequency of the inverters, MPP controllers, sudden dc system changes, partial shading and irradiance changes, crosstalk, simultaneous inverter operations, start-up conditions, PV degradation like aging, and sensor inaccuracy.

In total, 270 unwanted tripping conditions were generated under various weather conditions ranging from partly cloudy and sunny weather between the months of July and November. The tuned algorithm can successfully avoid 100% of unwanted tripping conditions.

VI. Conclusion and Future Works

A new series PV arc fault detection algorithm has been proposed which can successfully detect arc faults without a priori knowledge of the PV system. Arc faults on different PV configurations of 6 PV modules or 12 PV modules in series with either 1 other parallel strings or no parallel strings, respectively, have successfully been detected. In addition, an arc fault generated on a completely unknown PV configuration with a 3-phase inverter has been tested using data provided by Sandia National Laboratories and successfully detected without changing or tuning any parameters from the Northeastern University experimental setup. Therefore, the detection algorithm is versatile in detecting arc faults with different PV configurations, independent of the PV parameters.

Through current demodulation and the extraction of the full arc fault noise spectrum describing pink noise, the arc fault detection algorithm can successfully isolate arc fault noise from other background noise. The detection algorithm avoided unwanted tripping scenarios caused by different switching frequencies, dc disconnect switch operations, fast partial shading conditions, and crosstalk across different PV strings.

In future research, different PV configurations involving module-level dc/dc converters and inverters, multiple MPPT, large parasitic inductance and capacitance masking should also be tested [35]. Lastly, the detection algorithm can be implemented in a digital signal processor (DSP) to accurately determine the trip time by also including the processing time of the arc fault detection device on fast DSP's.

Acknowledgment

The authors gratefully acknowledge the data provided by Sandia National Laboratories.

References

[1] M. K. Alam, F. Khan, J. Johnson, and J. Flicker, "A comprehensive review of catastrophic faults in PV arrays: Types, detection, and mitigation techniques," *IEEE J. Photovolt.*, vol. 5, no. 3, pp. 982–997, May 2015.

[2] S. Lu, B. T. Phung, and D. Zhang, "A comprehensive review on DC arc faults and their diagnosis methods in photovoltaic systems," *Renewable Sustain., Energy Rev.*, vol. 89, pp. 88–98, Jun. 2018.

[3] J. Johnson, K. M. Armijo, M. Avrutsky, D. Eizips, and S. Kondrashov, "Arc-fault unwanted tripping survey with UL 1699B-listed products," in *Proc. IEEE 42nd Photovolt. Spec. Conf.*, 2015, pp. 1–6.

[4] S. Chen, X. Li, and J. Xiong, "Series arc fault identification for photovoltaic system based on time-domain and time-frequency-domain analysis," *IEEE J. Photovolt.*, vol. 7, no. 4, pp. 1105–1114, Jul. 2017.

[5] F. Erhard, B. Schaller, and F. Berger, "Field test results of serial DC arc fault investigations on real photovoltaic systems," in *Proc. 49th Int. Universities Power Eng. Conf.*, 2014, pp. 1–6, doi: 10.1109/UPEC.2014.6934689.

[6] J. Johnson and J. Kang, "Arc-fault detector algorithm evaluation method utilizing prerecorded arcing signatures," in *Proc. 38th IEEE Photovolt. Spec. Conf.*, 2012, pp. 1378–1382.

[7] D. A. Dini, P. W. Brazis, and K.-H. Yen, "Development of arc-fault circuit-interrupter requirements for photovoltaic systems," in *Proc. IEEE 37th Photovolt. Spec. Conf.*, 2011, pp. 001790–001794, doi: 10.1109/PVSC.2011.6186301.

[8] J. Johnson, S. Kuszmaul, W. Bower, and D. Schoenwald, "Using PV module and line frequency response data to create robust arc fault," in *Proc. 26th Eur. Photovolt. Sol. Energy Conf.*, 2011, pp. 3745–3750.

[9] J. Johnson, C. Oberhauser, M. Montoya, A. Fresquez, S. Gonzalez, and A. Patel, "Crosstalk nuisance trip testing of photovoltaic DC arc-fault detectors," in *Proc. IEEE 39th Photovolt. Spec. Conf.*, 2012, pp. 001383–001387.

[10] N. L. Georgijevic, M. V. Jankovic, S. Srdic, and Z. Radakovic, "The detection of series arc fault in photovoltaic systems based on the arc current entropy," *IEEE Trans. Power Electron.*, vol. 31, no. 8, pp. 5917–5930, Aug. 2016.

[11] J. C. Kim, B. Lehman, and R. Ball, "A series DC arc fault detection algorithm based on PV operating characteristics and detailed extraction of pink noise behavior," in *Proc. IEEE Appl. Power Electron. Conf. Expo.*, 2021, pp. 989–994, doi: 10.1109/APEC42165.2021.9487451.

[12] J. Johnson and K. Armijo, "Parametric study of PV arc-fault generation methods and analysis of conducted DC spectrum," in *Proc. IEEE 40th Photovolt. Spec. Conf.*, 2014, pp. 3543–3548, doi: 10.1109/PVSC.2014.6924874.
[13] M. Zhen, W. Li, and S. Qiangang, "The characteristics of DC arc faults current," in *Proc. 15th Eur. Conf. Power Electron. Appl.*, 2013, pp. 1–9, doi: 10.1109/EPE.2013.6631914.
[14] S. McCalmont, "Low cost arc fault detection and protection for PV systems," National Renewable Energy Laboratory, Tigo Energy,Los Gatos, CA, USA, Tech. Rep. NREL/SR-5200-60660, 2013.
[15] J. Johnson et al., "Photovoltaic DC arc fault detector testing at sandia national laboratories," in *Proc. IEEE 37th Photovolt. Spec. Conf.*, 2011, pp. 003614–003619.
[16] Z. Wang and R. S. Balog, "Arc fault and flash signal analysis in DC distribution systems using wavelet transformation," *IEEE Trans. Smart Grid*, vol. 6, no. 4, pp. 1955–1963, Jul. 2015.
[17] A. Pamer, G. Ritzberger, and F. Oberzaucher, "Method for detecting arcs in photovoltaic systems and such a photovoltaic system," US Patent WO2016037897A1, Nov. 5, 2013.
[18] X. Yao, L. Herrera, S. Ji, K. Zou, and J. Wang, "Characteristic study and time-domain discrete- wavelet-transform based hybrid detection of series DC arc faults," *IEEE Trans. Power Electron.*, vol. 29, no. 6, pp. 3103–3115, Jun. 2014.
[19] H.-P. Park and S. Chae, "DC series arc fault detection algorithm for distributed energy resources using arc fault impedance modeling," *IEEE Access*, vol. 8, pp. 179039–179046, 2020.
[20] Y. Abdullah et al., "Hurst-exponent-based detection of high-impedance DC arc events for 48-V systems in vehicles," *IEEE Trans. Power Electron.*, vol. 36, no. 4, pp. 3803–3813, Apr. 2021.
[21] W. Gao and R.-J. Wai, "Series arc fault detection of grid-connected pv system via SVD denoising and IEWT-TWSVM," *IEEE J. Photovolt.*, vol. 11, no. 6, pp. 1493–1510, Nov. 2021.
[22] H. Wang et al., "DC series arc fault detection method in photovoltaic system based on multiple frequency selections for common-mode conductive voltage," *IEEE Trans. Power Electron.*, vol. 37, no. 12, pp. 15538–15553, Dec. 2022.
[23] V. Le, X. Yao, C. Miller, and B.-H. Tsao, "Series DC arc fault detection based on ensemble machine learning," *IEEE Trans. Power Electron.*, vol. 35, no. 8, pp. 7826–7839, Aug. 2020.
[24] S. Lu, A. Sahoo, R. Ma, and B. T. Phung, "DC series arc fault detection using machine learning in photovoltaic systems: Recent developments and challenges," in *Proc. 8th Int. Conf. Condition Monit. Diagnosis*, 2020, pp. 416–421, doi: 10.1109/CMD48350.2020.9287192.
[25] H.-P. Park, M. Kim, and S. Chae, "Smart DC optimizer for DC series arc fault detection and extinguishing," *IEEE Trans. Power Electron.*, vol. 37, no. 9, pp. 10117–10121, Sep. 2022.
[26] J. C. Kim, B. Lehman, and R. Ball, "Series PV arc fault detection using current demodulation and autocorrelation coefficients," in *Proc. IEEE Energy Convers. Congr. Expo.*, 2022, pp. 1–7, doi: 10.1109/ECCE50734.2022.9947524.
[27] H.-P. Park, M. Kim, J.-H. Jung, and S. Chae, "Series DC arc fault detection method for PV systems employing differential power processing structure," *IEEE Trans. Power Electron.*, vol. 36, no. 9, pp. 9787–9795, Sep. 2021.
[28] S. Chae, J. Park, and S. Oh, "Series DC arc fault detection algorithm for DC microgrids using relative magnitude comparison," *IEEE J. Emerg. Sel. Topics Power Electron.*, vol. 4, no. 4, pp. 1270–1278, Dec. 2016.
[29] H. Zhu, Z. Wang, and R. S. Balog, "Real time arc fault detection in PV systems using wavelet decomposition," in *Proc. IEEE 43rd Photovolt. Spec. Conf.*, 2016, pp. 1761–1766, doi: 10.1109/PVSC.2016.7749926.
[30] Y. Abdullah, B. Hu, Z. Wei, J. Wang, and A. Emrani, "Adaptive detection of DC arc faults based on hurst exponents and current envelope," in *Proc. IEEE Appl. Power Electron. Conf. Expo.*, 2018, pp. 3392–3397, doi: 10.1109/APEC.2018.8341590.
[31] J. C. Kim, B. Lehman, and R. Ball, "DC arc fault model superimposing multiple random arc noise states on an average model," in *Proc. 20th Workshop Control Model. Power Electron.*, 2019, pp. 1–8, doi: 10.1109/COMPEL.2019.8769649.
[32] R. F. Ammerman, T. Gammon, P. K. Sen, and J. P. Nelson, "DC-arc models and incident-energy calculations," *IEEE Trans. Ind. Appl.*, vol. 46, no. 5, pp. 1810–1819, Sep./Oct. 2010.
[33] F. Schimpf and L. E. Norum, "Recognition of electric arcing in the DC-wiring of photovoltaic systems," in *Proc. 31st Int. Telecommun. Energy Conf.*, 2009, pp. 1–6, doi: 10.1109/INTLEC.2009.5352037.
[34] Y. Zhao, F. Balboni, T. Arnaud, J. Mosesian, R. Ball, and B. Lehman, "Fault experiments in a commercial-scale PV laboratory and fault detection using local outlier factor," in *Proc. IEEE 40th Photovolt. Spec.t Conf.*, 2014, pp. 3398–3403, doi: 10.1109/PVSC.2014.6925661.
[35] R. K. Pearson, *Mining Imperfect Data: Dealing with Contamination and Incomplete Records*. Philadelphia, PA, USA: Soc. Ind. Appl. Math., 2005.
[36] C. Strobl and P. Meckler, "Arc faults in photovoltaic systems," in *Proc. 56th IEEE Holm Conf. Elect. Contacts*, 2010, pp. 1–7.
[37] B. Novak, *Implementing Arc Detection in Solar Applications: Achieving Compliance With the New UL 1699B Standard*. Dallas, TX, USA: Texas Instrument, 2012.
[38] K. Xia, Z. He, Y. Yuan, Y. Wang, and P. Xu, "An arc fault detection system for the household photovoltaic inverter according to the DC bus currents," in *Proc. 18th Int. Conf. Elect. Mach. Syst.*, 2015, pp. 1687–1690, doi: 10.1109/ICEMS.2015.7385312.
[39] G. Seo, H. Bae, B. Cho, and K. Lee, "Arc protection scheme for DC distribution systems with photovoltaic generation," in *Proc. Int. Conf. Renewable Energy Res. Appl.*, 2012, pp. 1–5.
[40] G. Seo, K. A. Kim, K. Lee, K. Lee, and B. Cho, "A new DC arc fault detection method using DC system component modeling and analysis in low frequency range," in *Proc. IEEE Appl. Power Electron. Conf. Expo.*, 2015, pp. 2438–2444, doi: 10.1109/APEC.2015.7104690.
[41] S. Chen and X. Li, "PV series arc fault recognition under different working conditions with joint detection method," in *Proc. IEEE 62nd Holm Conf. Elect. Contacts*, 2016, pp. 25–32.
[42] H. Braun et al., "Signal processing for fault detection in photovoltaic arrays," in *Proc. IEEE Int. Conf. Acoust., Speech Signal Process.*, 2012, pp. 1681–1684.
[43] S. Changali et al., "Parallel arc detection using discrete wavelet transforms," US Patent 0 165 521 A1, Jul. 1, 2010.
[44] C. He, L. Mu, and Y. Wang, "The detection of parallel arc fault in photovoltaic systems based on a mixed criterion," *IEEE J. Photovolt.*, vol. 7, no. 6, pp. 1717–1724, Nov. 2017.
[45] Y. Guo, L. Wang, Z. Wu, and B. jiang, "Wavelet packet analysis applied in detection of low-voltage DC arc fault," in *Proc. IEEE 4th Conf. Ind. Electron. Appl.*, 2009, pp. 4013–4016.
[46] X. Yao, L. Herrera, and J. Wang, "DC arc fault detection method and hardware implementation," in *Proc. IEEE 28th Annu. Appl. Power Electron. Conf. Expo.*, 2013, pp. 2444–2449.
[47] Y. Gao, J. Zhang, Y. Lin, and Y. Sun, "An innovative photovoltaic DC arc fault detection method through multiple criteria algorithm based on a new arc initiation method," in *Proc. IEEE 40th Photovolt. Spec. Conf.*, 2014, pp. 3188–3192, doi: 10.1109/PVSC.2014.6925613.
[48] X. Yao, L. Herrera, and J. Wang, "Impact evaluation of series dc arc faults in dc microgrids," in *Proc. IEEE Appl. Power Electron. Conf. Expo.*, 2015, pp. 2953–2958, doi: 10.1109/APEC.2015.7104771.
[49] H. Haeberlin and M. Real, "Arc detector for remote detection of dangerous arcs on the DC side of PV plants," in *Proc. 22nd Eur. Photovolt. Sol. Energy Conf.*, 2007, pp. 1–6.
[50] S. Lu, T. Sirojan, B. T. Phung, D. Zhang, and E. Ambikairajah, "DA-DCGAN: An effective methodology for DC series arc fault diagnosis in photovoltaic systems," *IEEE Access*, vol. 7, pp. 45831–45840, 2019.
[51] J. Yang and Y. Wang, "Identification and detection of DC arc fault in photovoltaic power generation system," in *Proc. Int. Conf. Intell. Transp., Big Data Smart City*, 2020, pp. 440–444.
[52] F. M. Uriarte et al., "A DC arc model for series faults in low voltage microgrids," *IEEE Trans. Smart Grid*, vol. 3, no. 4, pp. 2063–2070, Dec. 2012.
[53] M. K. Alam, F. Khan, J. Johnson, and J. Flicker, "PV arc-fault detection using spread spectrum time domain reflectometry (SSTDR)," in *Proc. IEEE Energy Convers. Congr. Expo.*, 2014, pp. 3294–3300.
[54] *Standard for Safety Photovoltaic (PV) DC Arc-Fault Circuit Protection*, UL 1699B, 2018.